# Multi-azimuth coherence

*Jie Qi*, The University of Oklahoma; Hanming Gu, The China University of Geosciences-Wuhan; Fangyu Li, and Kurt Marfurt, The University of Oklahoma.*

**Summary**

With the interest to map azimuthal variation of horizontal stress as well as to improve the signal-to-noise ratio of unconventional resource plays, wide/full azimuth seismic data acquisition has become common. Migrating seismic traces into different azimuthal bins costs no more than migrating them into one bin. If velocity anisotropy is not taken into account by the migration algorithm, subtle discontinuities and some major faults may exhibit lateral shifts, resulting in a smeared image after stacking. Based on these two issues, we introduce a new way to compute coherence for azimuthally limited data volumes. Like multispectral coherence, we modify the covariance matrix to be the sum of the covariance matrix of each azimuthally limited volume, then use the integrated covariance matrix to compute the coherent energy.

**Introduction**

Seismic attributes are routinely used to quantify changes in amplitude, dip, and reflector continuity in seismic amplitude volumes. Coherence is an edge-detection attribute that maps lateral changes in waveform, which may be due to structural discontinuities, stratigraphic discontinuities, pinchouts, or steeply dipping coherent noise cutting more gently dipping reflectors. Several generations of coherence algorithm have been introduced and applied to geological discontinuity detection, including the cross-correlation (Bahorich and Farmer, 1995), the semblance (Marfurt et al., 1998), the eigenstructure method (Gersztenkorn and Marfurt, 1999), the gradient structure tensor (Bakker, 2002), and the predictive error filtering (Bednar, 1998) algorithms. All those algorithms operate on a spatial window of neighboring traces (Chopra and Marfurt, 2007).

After picking faults directly on vertical slices through the seismic amplitude volume, the coherence family of attributes is the most popular tool to map faults on seismic time, horizon, and stratal slices. Coherence also delineates channel edges, carbonate build-ups, slumps, collapse features and angular unconformities (e.g. Sullivan et al., 2006; Schuelke, 2011; Qi et al., 2014; Qi et al., 2016).

The energy-ratio coherence algorithm (Chopra and Marfurt, 2007) also used a covariance matrix, but now computed from windowed analytic traces (the original data and its Hilbert transform), and estimates the coherent component of the data using a Karhunen-Loeve filter. Like semblance, in this algorithm, the coherence is the ratio of the energy of the coherent (KL-filtered) analytic traces to that of the original analytic traces. Bakker (2002) computed a version of coherence called "chaos" by computing eigenvalues of the gradient structure tensor. The 3x3 gradient structure tensor is computed by cross-correlating derivatives of the seismic amplitude in the x, y, and z directions. The first eigenvalue represents the energy of the data variability (or gradient) perpendicular to reflector dip. If the data can be represented by a constant amplitude planar event, the chaos = -1.0. In contrast, if the data are totally random, the chaos = +1.0. Closely related to coherence is Luo et al.'s (2003) filter algorithm, generalized to work at longer wavelength's as a generalized Hilbert transform (Luo et al., 2003). Kington (2015) compared different coherence algorithms and exhibited the trade-offs among different implementations.

Li and Lu (2014), and Li et al. (2015) computed coherence from different spectral components and co-rendered them using an RGB color model. Sui et al. (2015) added a covariance matrices computed from a suite of spectral magnitude components, obtaining a coherence image superior to that of the original broad-band data. Marfurt (2017) expanded on this idea, but added coherence matrices computed from analytic spectral components (the spectral voices and their Hilbert transforms) along structural dip and found improved suppression of random noise and enhancement of small faults and karst collapse features.

In this paper, we build on this last piece of work, but now generalize it to sum a covariance matrices computed from a suite of azimuthally limited rather than frequency limited volumes. We begin our paper with a review of the energy ratio coherence algorithm. We show the improved lateral resolution but reduced signal-to-noise of coherence images generated from azimuthally limited seismic data. We then show how the multi-azimuth coherence computation provides superior results when applied to a data volume that has been properly migrated using an azimuthally varying velocity model. Next, we apply the multi-azimuth coherence algorithm to a data volume that has not been properly corrected for azimuthal anisotropy. We conclude with a summary of our findings and a short list of recommendations.

**Method**

Coherence is an edge-detection attribute, and measures lateral changes in the seismic waveform and amplitude. The covariance matrix is constructed

from a suite of sample vectors, each parallel to structural dip. Figure 1 shows $2K$+1=7 sample vectors of length $M$=5, or one sample for each trace. The covariance matrix for this data window is

$$C_{mn} = \sum_{k=-K}^{+K} \left(d_{km} d_{kn} + d_{km}^{H} d_{kn}^{H}\right), \qquad (1)$$

where the superscript H denotes the Hilbert transform, and the subscripts $m$ and $n$ are indices of input traces. The Hilbert transformed (90° phase rotated) sample vectors don't modify the vertical resolution, but improve areas of low signal-to-noise ratio about zero crossing (Gersztenkorn and Marfurt, 1999; Marfurt, 2006). The first eigenvector $\mathbf{v}^{(1)}$ of the matrix **C** best represents the lateral variation of each of the sample vectors. In Figure 1b, each sample vector is an approximate reflects a scaled version of the pattern (2, 2, 2, 1, 1), where the scaling factor can be positive for a peak, negative for a trough, or zero for a zero crossing. The first eigenvector for this cartoon will be a unit length vector representing this pattern:

$$\mathbf{v}^{(1)} = \left(\tfrac{2}{\sqrt{14}}\ \tfrac{2}{\sqrt{14}}\ \tfrac{2}{\sqrt{14}}\ \tfrac{1}{\sqrt{14}}\ \tfrac{1}{\sqrt{14}}\right). \qquad (2)$$

Cross correlating this eigenvector with the $k^{th}$ sample vector that includes the analysis point gives a cross-correlation coefficient, $\beta_k$:

$$\beta_k = \sum_{m=1}^{M} d_{km} v_m^{(1)}, \qquad (3)$$

The Karhunen-Loève filtered data within the analysis window are then:

$$d_{km}^{KL} = \beta_k v_m^{(1)}. \qquad (4)$$

Note that in Figure 1b that the wavelet amplitude of the three left most traces is about two times larger than that of the two right-most traces.

Energy ratio coherence computes the ratio of coherent energy and total energy in an analysis window:

$$C_{ER} = \frac{E_{coh}}{E_{tot} + \varepsilon^2}, \qquad (5)$$

where the coherent energy $E_{coh}$ (the energy of the KL-filtered data) is:

$$E_{coh} = \sum_{k=-K}^{+K} \sum_{m=1}^{M} \left[\left(d_{km}^{KL}\right)^2 + \left(d_{km}^{H\,KL}\right)^2\right], \qquad (6)$$

while the total energy $E_{tot}$ of unfiltered data in the analysis window is:

$$E_{tot} = \sum_{k=-K}^{+K} \sum_{m=1}^{M} \left[(d_{km})^2 + \left(d_{km}^{H}\right)^2\right], \qquad (7)$$

and where a small positive value, $\varepsilon$, prevents division by zero.

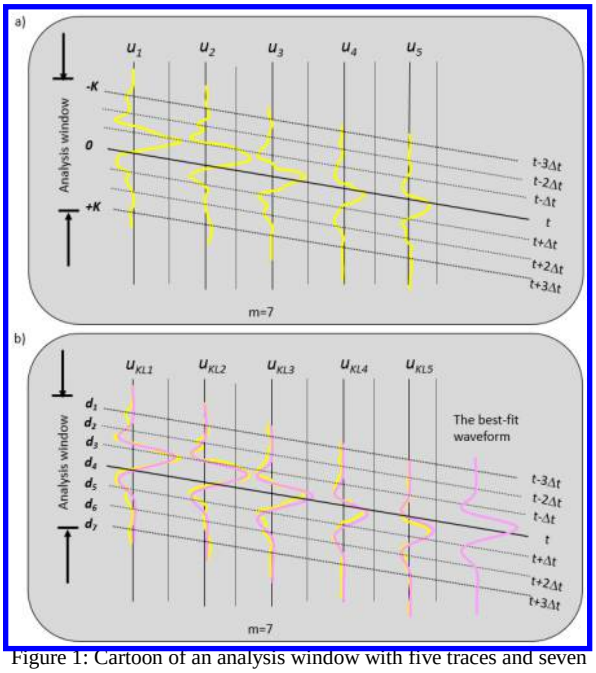


Figure 1: Cartoon of an analysis window with five traces and seven samples. Note that the wavelet amplitude of the three left most traces is about two times larger than that of the two right-most traces.

We generalize the concept of energy ratio coherence by summing $J$ covariance matrices $\mathbf{C}(\varphi_j)$ computed from each of the $J$ azimuthally-sectored data volumes:

$$\mathbf{C}_{multi-\varphi} = \sum_{j=1}^{J} \mathbf{C}(\varphi_j). \qquad (8)$$

The summed covariance matrix is of the same $M$ by $M$ size as the original single azimuth covariance matrix but is now composed of $J$ time as many sample vectors. Eigen-decomposition of the covariance matrix is a nonlinear process, such that the first eigenvector of the summed covariance matrix is not a linear combination of the first eigenvectors computed for the azimuthally limited covariance matrix, in which case the resulting coherence would be the average of the azimuthally limited coherence computations. To minimize the volume of data to be analyzed, azimuths are

commonly binned into six $30^0$ or eight $22.5^0$ sectors, although finer binning is common in large processing shops.

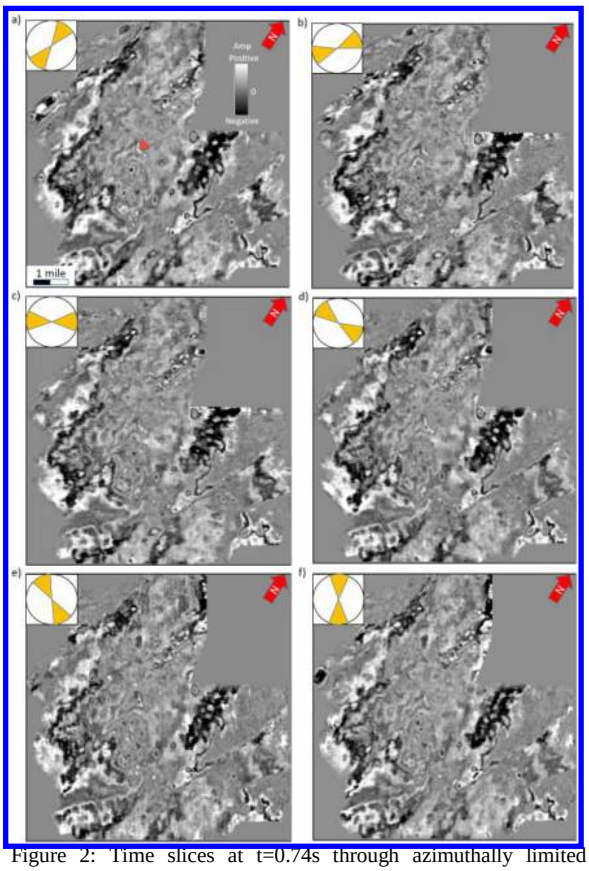


Figure 2: Time slices at t=0.74s through azimuthally limited migrated seismic amplitude volumes: (a) 165o to 15o, (b) 15o to 45o, (c) 45o to 75o, (d) 75o to 105o, (e) 105o to 135o, and (f) 135o to 165o. Note azimuthal variations and that although the signal-to-noise ratio of each azimuthal sector is low, one can identify faults and karst features.

**Application**

Our example is from the Fort Worth Basin, Texas. The dataset was acquired in 2006 using 16 live receiver lines forming a wide-azimuth survey with a nominal 55×55 ft CDP bin size. The data were preprocessed and binned into six azimuths, preserving amplitude fidelity at each step prior to prestack time migration (Roende et al., 2008). Figure 2 shows time slices at t=0.74 s through the six different azimuthally limited seismic amplitude volumes. Figure 3 shows time slices through the six corresponding coherence volumes. Because the signal-to-noise ratio of each azimuthal sector seismic amplitude is low, the signal-to-noise ratio of the resulting coherence images are also low. Those differences between the azimuthally limited coherence images include the shape and size of karst features (indicated by green arrows), the continuity of subtle faults (indicated by yellow arrows), and level of incoherent noise. Zhang et al., (2014), Zhang et al. 2015, and Verma et al., (2016) applied a prestack structure oriented filter to this dataset that suppresses coherent acquisition, processing, and migration artifacts. As recognized by Perez and Marfurt (2008) faults are best delineated by the azimuths perpendicular to them (e.g. Figure 3a at $0^o$ vs. Figure 3c at $60^o$)

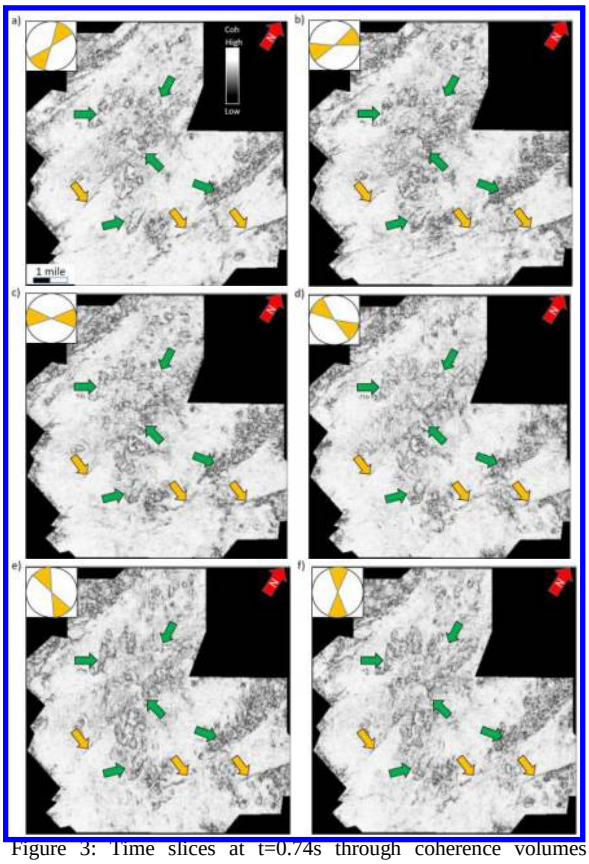


Figure 3: Time slices at t=0.74s through coherence volumes computed from the azimuthally limited data shown in Figure 1: (a) $165^o$ to $15^o$, (b) $15^o$ to $45^o$, (c) $45^o$ to $75^o$, (d) $75^o$ to $105^o$, (e) $105^o$ to $135^o$, and (f) $135^o$ to $165^o$. Although one can identify faults (yellow arrows) and karst collapse features (green arrows), the images are quite noisy.

Stacking the six seismic amplitude volumes and then compute coherence (the conventional analysis workflow) gives the result shown in Figure 4a which exhibits greater signal-to-noise but slightly lower lateral resolution than the azimuthally limited coherence time slices shown in Figure 3. Figure 4b shows the result of stacking the six images shown in Figure 3. The signal-to-noise ratio on Figure 4b is

lower than that of Figure 4a, however edges of the karst features become appear more pronounced than on the traditional coherence computation. Figure 4c shows the multi-azimuth coherence result computed using the covariance matrix described by equation 8. Note that the multi-azimuth coherence displays the higher lateral resolution rather than either traditional coherence or the stacked azimuthal coherence. Karst features (indicated by green arrows) exhibit highly incoherent anomalies, and subtle faults (indicated by yellow arrows) appear as strong as major faults. Multi-azimuth coherence not only preserves most of the discontinuities seen in each of the azimuthally limited coherence volumes in Figure 3, but also suppresses incoherent noise.

## Conclusions

We have introduced a new way to compute coherence of azimuthal sectors that preserving subtle discontinuities, avoiding smearing lateral variations and suppressing incoherent noise. The main modification comparing to the energy-ratio coherence algorithm is that we integrate all weighted covariance of each azimuthal sectors together in one dip-scanning window, and then compute coherent energy of the covariance matrix. Eigen-decomposition of the summed covariance matrix of all azimuthally limited volumes is a nonlinear process, such that the first eigenvector of the summed covariance matrix is not a linear combination of the first eigenvectors computed for the azimuthally limited covariance matrix. In the implementation to azimuthal variation interpretation, the multi-azimuth coherence would be the average of the azimuthally limited coherence computations, but has the higher signal-to-noise ratio rather than each azimuthally limited coherence volumes. Comparing to traditional coherence or the stacked azimuthal coherence, the multi-azimuth coherence displays the higher lateral resolution, and exhibit karst collapse features and subtle faults as strong as major faults. In low signal-to-noise ratio dataset, the multi-azimuth coherence not only preserves most of the discontinuities seen in each of the azimuthally limited coherence volumes, but also suppresses incoherent noise.

## Acknowledgements

The authors would like to thank Marathon Oil for providing the data. We also thank all financial support by the University of Oklahoma Attribute-Assisted Seismic Processing and Interpretation (consortium).

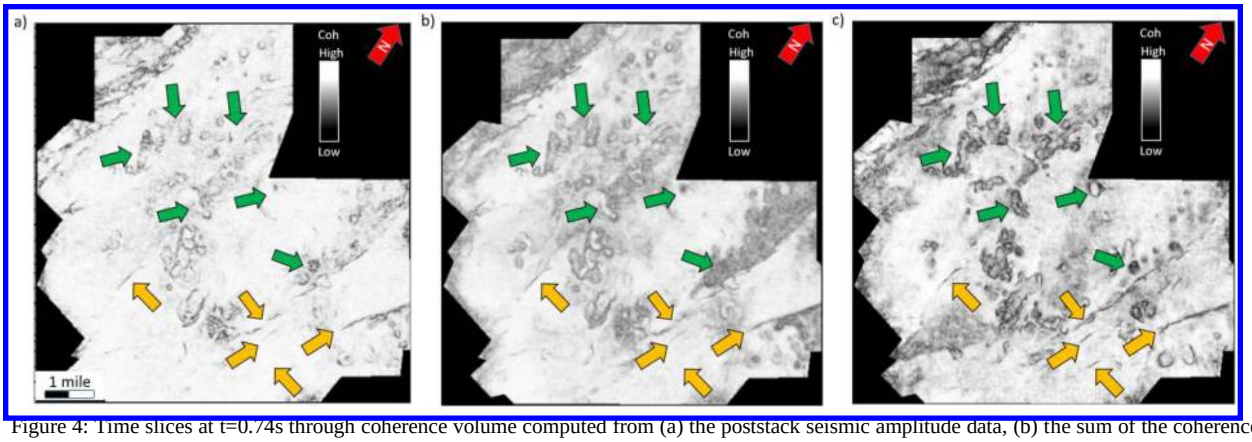


Figure 4: Time slices at t=0.74s through coherence volume computed from (a) the poststack seismic amplitude data, (b) the sum of the coherence shown in Figure 2, and (c) the multi-azimuth coherence. Note there is the improved lateral resolution of the multi-azimuth coherence. Edges of karst features (indicated by green arrows) are better delineated, and subtle discontinuities (indicated by yellow arrows) are as strong as major faults. The result obtained by stacking the azimuthal coherence volumes is as same places noisy and in other slices.

**EDITED REFERENCES**

Note: This reference list is a copyedited version of the reference list submitted by the author. Reference lists for the 2017 SEG Technical Program Expanded Abstracts have been copyedited so that references provided with the online metadata for each paper will achieve a high degree of linking to cited sources that appear on the Web.

**REFERENCES**


Bahorich, M. S., and S. L. Farmer, 1995, 3-D seismic discontinuity for faults and stratigraphic features: The Leading Edge, **14**, 1053–1058, http://doi.org/10.1190/1.1437077.

Bakker, P., 2002, Image structure analysis for seismic interpretation: PhD thesis, Delft University of Technology.

Chopra, S., K. J. Marfurt, 2007, Seismic attributes for prospect identification and reservoir characterization: Book, SEG, https://doi.org/10.1190/1.9781560801900.

Gersztenkorn, A., and K. J. Marfurt, 1999, Eigenstructure based coherence computations as an aid to 3D structural and stratigraphic mapping: Geophysics, **64**, 1468–1479, http://doi.org/10.1190/1.1444651.

Kington, J., 2015, Semblance, coherence, and other discontinuity attributes: The Leading Edge, **34**, 1510–1512, http://doi.org/10.1190/tle34121510.1.

Li, F., J. Qi, and K. J. Marfurt, 2015, Attribute mapping of variable thickness incised valley-fill systems: The Leading Edge, **34**, 48–52, http://doi.org/10.1190/tle34010048.1.

Li, F., and W. Lu, 2014, Coherence attribute at different spectral scales: Interpretation, **2**, 1–8, http://doi.org/10.1190/INT-2013-0089.1.

Luo, Y., S. Al-Dossary, M. Marhoon, and M. Alfaraj, 2003, Generalized Hilbert transform and its application in geophysics: The Leading Edge, **22**, 198–202, http://doi.org/10.1190/1.1564522.

Marfurt, K. J., 2017, Interpretational value of multispectral coherence: 79th Annual International Conference and Exhibition, EAGE, Extended Abstracts.

Marfurt, K. J., 2006, Robust estimates of 3D reflector dip and azimuth: Geophysics, **71**, no. 4, P29–P40, http://doi.org/10.1190/1.2213049.

Marfurt, K. J., R. L. Kirlin, S. H. Farmer, and M. S. Bahorich, 1998, 3D seismic attributes using a running window semblance-based algorithm: Geophysics, **63**, 1150–1165, http://doi.org/10.1190/1.1444415.

Perez, G., and K. J. Marfurt, 2008, Warping prestack imaged data to improve stack quality and resolution: Geophysics, **73**, no. 2, P1–P7, http://doi.org/10.1190/1.2829986.

Qi, J., T. Lin, T. Zhao, F. Li, and K. J. Marfurt, 2016, Semisupervised multiattribute seismic facies analysis: Interpretation, **4**, SB91–SB106, http://doi.org/10.1190/INT-2015-0098.1.

Qi, J., B. Zhang, H. Zhou, and K. J. Marfurt, 2014, Attribute expression of fault-controlled karst — Fort Worth Basin, TX: Interpretation, **2**, SF91–SF110, http://doi.org/10.1190/INT-2013-0188.1.

Roende, H., C. Meeder, J. Allen, S. Peterson, and D. Eubanks, 2008, Estimating subsurface stress direction and intensity from subsurface full-azimuth land data: 78th Annual International Meeting, SEG, Expanded Abstracts, 217–220, http://doi.org/10.1190/1.3054791.

Schuelke, J. S., 2011, Overview of seismic attribute analysis in shale play: Attributes: New views on seismic imaging-Their use in exploration and production: Presented at the 31st Annual GCSSEPM Foundation Bob F. Perkins Research Conference.

Sui, J.-K., X. Zheng, and Y. Li, 2015, A seismic coherency method using spectral attributes: Applied Geophysics, **12**, no. 3, 353–361, http://doi.org/10.1007/s11770-015-0501-5.

Sullivan, E. C., K. J. Marfurt, A. Lacazette, and M. Ammerman, 2006, Application of new seismic attributes to collapse chimneys in the Fort Worth basin: Geophysics, **71**, no. 4, B111–B119, http://doi.org/10.1190/1.2216189.

Verma, S., S. Guo, and K. J. Marfurt, 2016, Data conditioning of legacy seismic using migration-driven 5D interpolation: Interpretation, **4**, SG31-SG40, http://doi.org/10.1190/INT-2015-0157.1.
Zhang, B., T. Zhao, J. Qi, and K. J. Marfurt, 2014, Horizon-based semiautomated nonhyperbolic velocity analysis: Geophysics, **79**, no. 6, U15–U23, http://doi.org/10.1190/geo2014-0112.1.
Zhang, B., D. Chang, T. Lin, and K. J. Marfurt, 2015, Improving the quality of prestack inversion by prestack data conditioning: Interpretation, **3**, T5–T12, http://doi.org/10.1190/INT-2014-0124.1.